IEEE Access
Multidisciplinary ⋮ Rapid Review ⋮ Open Access Journal

Received June 4, 2020, accepted June 23, 2020, date of publication July 2, 2020, date of current version July 27, 2020.

Digital Object Identifier 10.1109/ACCESS.2020.3006460

Measurement of Simulated Lunar Soil Information Using Rutting Images

HONGWEI GAO[1,2], YUQI ZHOU[1], YUEQIU JIANG[1], JIAHUI YU[1,3], ZHAOJIE JU[2,3,4], (Senior Member, IEEE), AND JINGUO LIU[2,4], (Senior Member, IEEE)

[1]School of Automation and Electrical Engineering, Shenyang Ligong University, Shenyang 110159, China
[2]State Key Laboratory of Robotics, Shenyang Institute of Automation, Chinese Academy of Sciences, Shenyang 110016, China
[3]School of Computing, University of Portsmouth, Portsmouth PO1 3HE, U.K.
[4]Institutes for Robotics and Intelligent Manufacturing, Chinese Academy of Sciences, Shenyang 110016, China

Corresponding authors: Zhaojie Ju (zhaojie.ju@port.ac.uk) and Jinguo Liu (liujinguo@sia.cn)

This work was supported in part by the Natural Science Foundation of China under Grant 51775541, in part by the National Key Research and Development Program of China under Grant 2018YFB1304600, in part by the CAS Interdisciplinary Innovation Team under Grant JCTD-2018-11, in part by the Liaoning Province Higher Education Innovative Talents Program Support Project under Grant LR2019058, and in part by the Liaoning Revitalization Talents Program under Grant XLYC1902095.

ABSTRACT Research on lunar soil has great value, and soil hardness is one of the essential parameters to be measured. Currently, the existing method involves contact measurement using special instruments. To reduce the self-weight and increase the scientific payloads of lunar rovers, a reanalysis of the data obtained from existing sensors provides a great solution for achieving different tasks. Therefore, a vision-based and noncontact method based on rutting images is proposed to estimate soil hardness. The overall approach includes two parts: rutting depth measurement and soil hardness measurement. To simulate a complex lunar environment, a variety of simulated lunar soil preparation schemes to achieve different soil states are designed in this paper. More importantly, this paper summarizes the empirical formulas of the simulated lunar soil in different states and the judgment conditions for defining the soil states based on the rutting depth. Finally, the accuracy, feasibility, and applicability of this method are verified. Experiments show the capability of the method we proposed to estimate soil hardness in simulated environments, as well as in the real lunar environment.

INDEX TERMS Rutting images, stereo vision, soil hardness, data reanalysis, simulated lunar soil.

I. INTRODUCTION

Lunar exploration is currently one of the most trending topics, and the surface soil of the moon has high scientific research value [1]. Therefore, understanding the properties of lunar soil has been the research focus of both institutions and engineers. As a special eye, the vision system of the lunar rover can obtain and analyse the surrounding information via pre-set methods [2], [3]. Moreover, the rutting can provide sufficient information about lunar soil parameters. Some studies have effectively combined these two perspectives [4], [5]. When the soil is deformed by the external force, it shows a series of mechanical properties, which can also be called physical mechanical properties of soil. Soil hardness as one of these parameters is originally used in agriculture, which can be described by the cone index, mechanical resistance and other forms. In order to unify the expression, this property is called soil hardness in this paper. With the cross development of science and technology, this property is also used in different fields. The hardness parameter, which is also one of the important parameters of lunar soil, can be used to assist the lunar rover performing more scientific tasks [6], [7]. In addition, the soil hardness parameter affects the determines of the rover's passability. Measuring the soil parameter around the rover is beneficial to the rover's optimal route planning, target capture [8] and risk aversion. It is necessary to further study the hardness of lunar soil.

Currently, the estimation methods of some lunar soil properties can be divided into two main categories; the first is the traditional contact measurement method [9]. In detail, the traditional method allows measurement tasks to be performed using a cone penetrometer. For example, Apollo 15 and 16 mission astronauts completed the manual measurements of soil parameters by using special instruments.

The associate editor coordinating the review of this manuscript and approving it for publication was Hossein Rahmani.

By comparison, indirect methods, as the second major category, have attracted more attention from scholars. Wang *et al.* [10] designed an ultrasonic measurement method, and Johnson *et al.* [11] achieved parameter estimation via spectrum technology. Unfortunately, using these expensive indirect measurement instruments usually increases the experimental cost and the difficulty of applying such methods in practical applications, so these studies have certain limitations. To enhance the work efficiency, unmanned geological investigations seem to have notable benefits. Therefore, using the existing parameters to achieve on-line soil property estimation in modelling methods is a popular approach. A model that can be used to estimate soil parameters with high accuracy was provided in study [11]. This method can identify the soil parameters based on in-situ data obtained from exploration rovers. Furthermore, Ding *et al.* [12] proposed a method for soil parameter estimation based on neural networks. These two on-line methods require large quantities of real data or many images to train the model, which may have a significant impact on the results when the training capacity is insufficient. In some studies [13]–[16], the soil parameters were determined by setting up a wheel-terrain interaction model, but the models discussed were based on the terra mechanics theory [17]. Practically, these studies estimated many soil mechanical parameters but did not consider the soil hardness parameter.

The lunar surface is usually covered with loose and fine particles, and the lunar rover can create ruts on the lunar soil [1], [11]. Improvements in vision techniques allow for more accurate assessments of rutting than those previously obtained. To increase the measurement accuracy, Kage and Matsushima [18] used four lasers and an in-vehicle binocular stereo to measure three-dimensional rutting information. Similarly, Kenarsari *et al.* [19] designed a three-camera structure to assess the rutting depth, area, and volume. However, the main drawback is that the two methods have very complex structural designs, and these algorithms are time-consuming. Based on an analysis of rutting images, a method of collecting real-time measurements of the rutting depth was proposed by Botha *et al.* [20], and this approach can be adopted to evaluate the safety of vehicles under different conditions. This method was tested on various terrains to verify its reliability and accuracy; nevertheless, it cannot be used for soil property detection, and there are many differences between planetary rovers and terrestrial vehicles [21]. Based on an extensive analysis of rutting information, Xue *et al.* [22] proposed a vision-based method for measuring wheel sinkage. This method can effectively identify the key parameters of multiple soil types, but it requires prior information about the environment, which is a great disadvantage when facing unknown complex environments. As China's first lunar rover, Yutu landed successfully on the moon and completed scientific missions [23]. Yutu was equipped with four kinds of scientific instruments, but did not have a professional soil measurement instrument, such as that on Apollo 15 [24], [25]. By summing up the experiences and lessons of Chang'E-3 mission, Chang'E-4 probe successfully landed in the lunar and began the scientific tasks [26]. Similarly, the vision system was one of the payloads of Chang'E-4 [27]. As described above, the application of visual system can be diversified. Therefore, to explore lunar soil information, the rutting images collected by the vision system provide significant reference value [3]. Practically, Gao *et al.* [9] used wheel sinkage to estimate the soil strength, and the method was verified with in situ soil penetrometer data from planet rovers. However, studies that have measured lunar soil hardness parameter are still relatively rare.

To solve the problems mentioned above, we propose an improved noncontact method for measuring lunar soil hardness. Based on the rutting images from Yutu, the depth of ruts can be measured via a binocular vision system, and the value of the lunar soil hardness can be obtained by our method. Additionally, according to the existing conditions, we design a set of realistic and feasible experimental schemes that have the characteristics of low cost, high efficiency, and simplicity. Therefore, the proposed method can provide an economical approach for studying the properties of lunar soil and performing planetary exploration. To effectively simulate the lunar soil environment, we design five different states and summarize ten judgment conditions between the different simulated lunar soil states and rutting depths. More importantly, we obtain the correlation between the rutting depth and the hardness value of the simulated lunar soil, and this correlation can help us apply the results of ground simulation experiments to environments on the lunar surface. Compared with the traditional contact method, our method can effectively reduce the energy consumption of the vehicular system and save space in the complex environment. In addition, our study can also provide some technical accumulation for the Chinese Lunar Exploration Program (CLEP).

The remainder of this paper is organized as follows: Section II introduces the rutting depth measurement system. In Section III, the proposed method is described in detail. The experimental results are shown in Section IV. Finally, the conclusion and future works are summarized in Section V.

II. VISUAL MEASUREMENT SYSTEM

This section describes the principle and implementation of the rutting depth measurement method, including the calibration of the binocular vision system, image processing methods, stereo matching and three-dimensional reconstruction, which provide the foundation for subsequent soil hardness estimation. The flow chart of the visual measurement system is shown in Fig.1.

A. CALIBRATION OF THE BINOCULAR VISION SYSTEM

The calibration of a binocular vision system can be subdivided into two parts. One part is camera calibration, which is used to obtain the internal parameters, external parameters and distortion parameters. The other part is the acquisition of camera structural parameters, which is used to describe

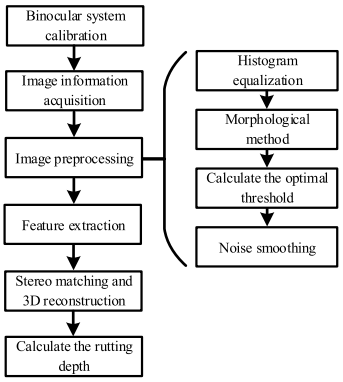

FIGURE 1. Flow chart of proposed visual rutting measurement system.

the spatial relationship between two cameras. In this study, we chose the CMOS industrial camera, which has a maximum resolution similar to that of Yutu, to simulate the actual working environment [28].

Camera calibration plays an extremely important role in a visual system, and the accuracy of calibration will directly affect the final three-dimensional reconstruction. Through calibration, the internal parameter matrix, which is only related to the physical structure of a camera, and the external parameter matrix can be obtained. The calibration method of camera parameters is not unique [29], [30], and the visual system used by Yutu was fixed to its mast [31], so the traditional calibration method can meet the corresponding demands. Compared with the proposed methods of Ito [32] and Faugeras [33] that used a linear technique to complete calibration, and a two-step calibration method [34], we finally use Zhang's calibration approach [35], which is easier to implement and yields higher accuracy. The camera model can be expressed as:

$$sp = C_{ip}C_{ep}P = \begin{bmatrix} k_x & k_s & u_0 & 0 \\ 0 & k_y & v_0 & 0 \\ 0 & 0 & 1 & 0 \end{bmatrix} \begin{bmatrix} R_c & t_c \\ 0 & 1 \end{bmatrix} P, \quad (1)$$

where s is the scale factor and p and P are the points the pixel coordinate system and the world coordinate system, respectively. To describe the relationship between the world coordinate system and the camera coordinate system, the external parameter matrix, C_{ep}, is composed of a rotation matrix R_c and a translation vector t_c. In addition, C_{ip} can be expressed as a 3×4 matrix and (u_0, v_0) are the coordinates of the principal point in equation (1); (k_x, k_y) are the focal ratios. A coupling effect may exist between the focal ratios, so we set the amplification factor k_s.

After obtaining the internal and external parameters of one camera, it is also necessary to determine the pose conversion relationship between two cameras, which is the structural parameter. With equation (2), the geometric relationship [18] between two cameras can be calculated as:

$$\begin{cases} R = R_{C1}R_{C2}^{-1} \\ t = t_{C1} - R_{C1}R_{C2}^{-1}t_{C2}, \end{cases} \quad (2)$$

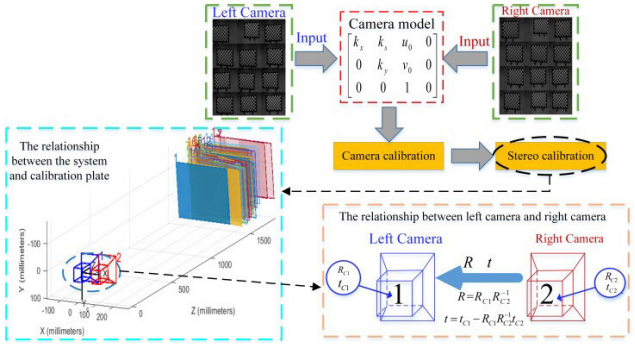

FIGURE 2. Relationships between the rutting depth and soil state.

TABLE 1. Calibration results of the camera parameters.

Parameters	Left Camera 1	Right Camera 2
(k_x, k_y)	(7354.813, 7356.916)	(1294.194, 980.395)
(u_0, v_0)	(1294.194,980.395)	(1301.662,979.451)
k_s	-3.702	-1.063
(k_1, k_2, k_3)	(-0.0884, 0.64572, 0.00079)	(-0.92092,0.61699,0.00144)
(p_1, p_2)	(0.00189, 0.00238)	(0.00147, 0.00184)

TABLE 2. Transformation from the right camera to the left camera.

	Transformation relation
R	$\begin{bmatrix} 0.99990 & -0.00069 & -0.01354 \\ 0.00037 & 0.99972 & -0.02373 \\ 0.01355 & 0.02372 & 0.99962 \end{bmatrix}$
t	$\begin{bmatrix} -100.773 & 1.229 & -0.868 \end{bmatrix}^T$

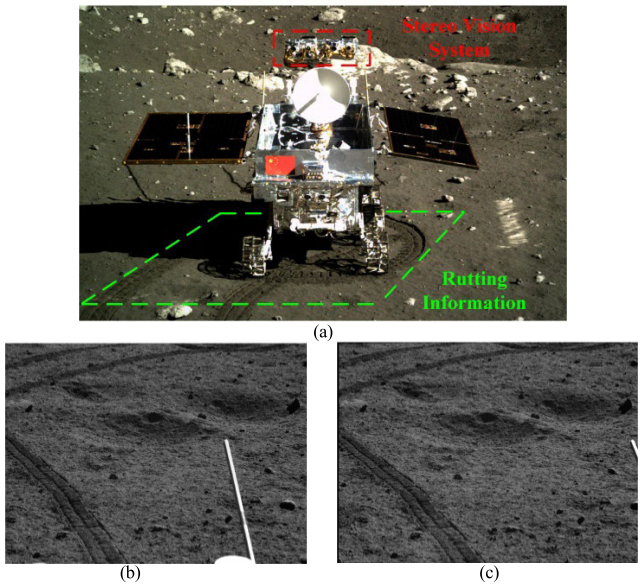

FIGURE 3. (a) Yutu lunar rover and vision system. (b) Image of right camera. (c) Image of left camera.

where R_{C1} and t_{C1} represent the external parameters of the left camera, R_{C2} and t_{C2} represent the external parameters

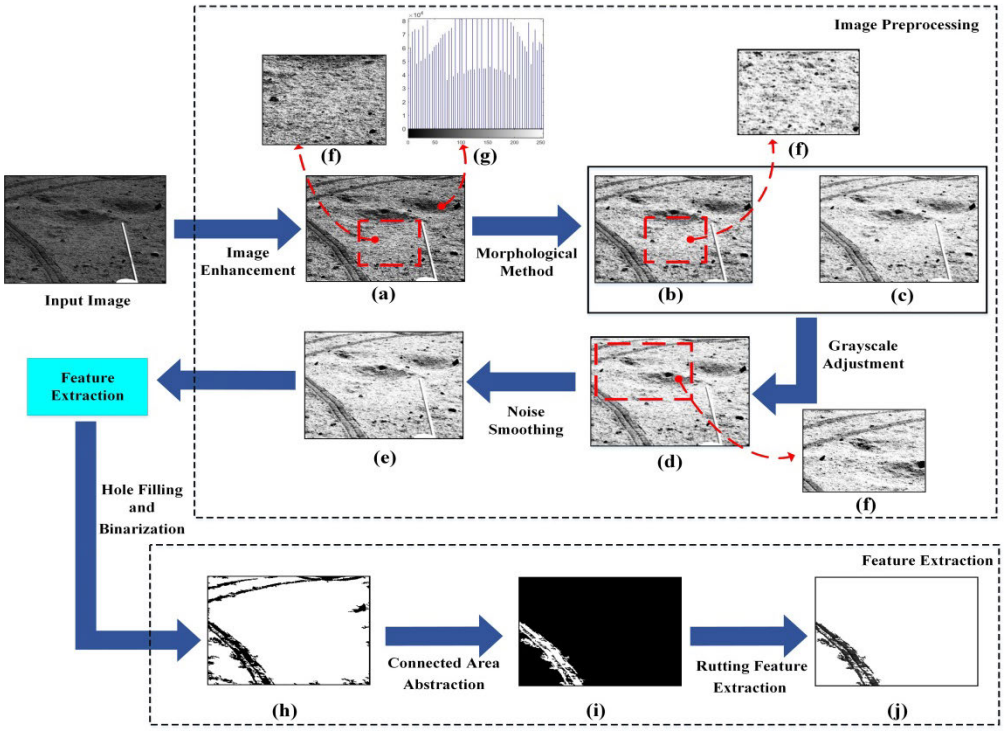

FIGURE 4. (a) and (g) Histogram equalization; (b)-(c) Morphological method; (d) Grey value adjustment step; (e) Noise smoothing; (f) Local magnification for observation; (h)-(j) Hole filling and binarization steps, connected area abstraction and feature extraction.

of the right camera, and the rotation matrix and translation vector can be obtained to complete the calibration of the binocular system [36].

In this study, we collect at least 85 pairs of calibration plate images of different positions and angles for the parameter solution to improve the calibration precision, and some of the collected images are shown in Fig. 2. The standard checker board [35] we used for camera calibration has a size of 400 mm × 300 mm with a 12×9 array, and the size of each chessboard is 30 mm × 30 mm. The complete calibration steps for the binocular vision system, the relative positions of the two cameras, and the relationship between the vision system and the calibration plate are shown in Fig. 2.

Some parameters are shown in Table 1, including the internal parameters; the radial distortion parameters k_1, k_2 and k_3; and the tangential distortion parameters p_1 and p_2.

In this paper, we set the relative distance between two cameras to be 100 mm, and it is worth noting that the distance between the cameras in Fig. 2 is also close to 100 mm. Table 2 shows the transformation relationship between two cameras. The absolute value of the first element of t is 100.773 mm, and its deviation from the actual value is only 0.773 mm.

B. IMAGE PROCESSING METHODS

In Fig. 3(a), we can see that the lunar rover leaves traces on the lunar surface, and the stereo vision system can capture images with ground information [29]. The original images transmitted by Yutu are shown in Fig. 3(b)-(c). Because of inevitable interference, it is not appropriate to directly perform stereo matching by using the collected images. Therefore, we design a reliable image processing method that mainly focuses on solving three problems during processing:

- Removing as much noise as possible;
- Avoiding or eliminating the effect of highlighting in the image;
- Accurately extracting the rutting information in the complex lunar environment.

The image processing operations are performed on the right image in Fig. 3, which is the same as the processes of the right image. Fig. 4 shows the overall process and effect of the rutting image processing. To the best of our knowledge, histogram equalization is one of the most popular image enhancement techniques, so we use standard histogram equalization methods to process the image [37], [38]. By reassigning the pixel grey values of the image, the grey values are evenly distributed in the new histogram, as shown in Fig. 4(a)(f)(g); the rutting information in the image is clearly distinguished from the lunar environment information. Second, the morphological method is used to optimize the small shadows after the equalization operation, as shown in Fig. 4(b)-(c). In Fig. 4(c), we use the expansion method to address the "black hole" that appears after a closed operation. Then, the particle swarm optimization algorithm is used to calculate the optimal threshold [39]. The number of iterations is 50, and the best threshold is 150. In Fig. 4(d)-(f), the image

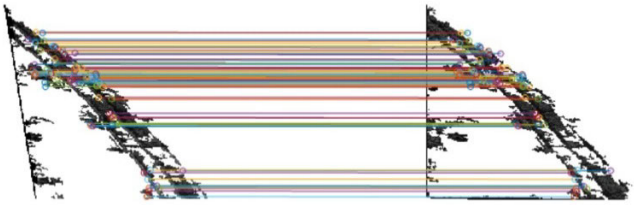

FIGURE 5. SURF feature matching.

segmentation effect is obvious. In addition, a Gaussian filter is used to smooth the images, as shown in Fig. 4(e).

To extract clear rutting information, feature extraction is an important step after image preprocessing. In Fig. 4(e), there are still some forms of interference, such as the lunar crater and lunar rocks, so we use the hole filling, binarization, and domain connectedness [40] methods to obtain the rutting information. These operations are shown in Fig. 4(h)-(j).

C. STEREO MATCHING AND 3D RECONSTRUCTION

Stereo matching is a key step in 3D reconstruction, and the epipolar rectification needs to be performed on the left and right images before matching. In our study, the purpose of the epipolar rectification is to avoid a full search when the feature points are matched to significantly improve the matching efficiency and reduce complexity. Be-cause the internal and external parameters of the experimental camera are known, we use the rectification method proposed by Fusiello *et al.* [41] to easily extract and correct the rutting information in subsequent ground simulated experiments. However, the external parameters cannot be obtained when the original images are transmitted by Yutu, so the weakly calibrated method is used to complete the rectification, for the rutting feature matching. For stereo matching, the RANSAC algorithm for the matching constraint is our preferred choice, and the epipolar rectification is also the constraint to solve the problems associated with potentially incorrect matches. Feature point detection should also be considered. Among the local feature detection algorithms, such as the scale-invariant feature transform (SIFT) [42], speeded up robust features (SURF) [42] and oriented fast and rotated brie (ORB) [44], we select SURF, which is more robust and faster than the other methods, to perform feature point matching. As shown in Fig. 5, the rutting information is matched after image processing, and the extracted feature points are scattered and covered most of the rutting information to meet the corresponding analysis requirements.

According to the imaging principle of a binocular vision system [36], if the internal and external parameters of two cameras are known, the three-dimensional coordinates of the measured points can be obtained by regression analysis using the least-squares method.

The edges of the rutting feature are the ground surface, and therefore, the ground can be fitted by the points at the edges. Therefore, the rutting depth is a distance between the point of the rutting feature and the fitting plane, as denoted by the following equation:

$$h = \frac{|A_1 x_0 + B_1 y_0 + C_1 z_0 + D_1|}{\sqrt{A_1^2 + B_1^2 + C_1^2}}, \tag{3}$$

where h is the rutting depth, (A_1, B_1, C_1, D_1) are the polynomial coefficients after least squares fitting, and (x_0, y_0, z_0) are the values of the three-dimensional coordinates.

III. HARDNESS MEASUREMENT SYSTEM BASED ON THE RUTTING DEPTH

The lunar surface is extremely complicated, and there is no model to accurately and quantitatively describe the lunar soil hardness. Therefore, we study the lunar soil information through purely empirical methods on the ground. At present, the common soil hardness tester measures the force by pushing a metal cone through the soil at a constant velocity, and the theoretical pressure gauge (kg/cm^2) is usually used to describe the result of measurement. The soil hardness can be measured directly by using a hardness tester, from which we can determine the loose condition of the soil at different depths. To ensure that the empirical formula obtained in experiments has high credibility, the following factors need to be considered:

- Various simulated lunar soil states to simulate the lunar environment;
- Many static pressure tests on the simulated lunar soil;
- Analyses of the simulated lunar soil in different layers;
- Relationships between the rutting depth and the simulated lunar soil hardness.

The soil condition on the lunar surface is not unique. In this paper, we simulated five states of the selected simulated lunar soil: the loose state, the relatively loose state, the natural state, the relatively compacted state and the compacted state. Based on the operation steps described in Fig. 6, the construction methods of the five states can be explained as follows.

A. DESIGN AND CONSTRUCTION OF FIVE SIMULATED LUNAR SOIL STATES

The soil condition on the lunar surface is not unique. In this paper, we simulated five states of the selected simulated lunar soil: the loose state, the relatively loose state, the natural state, the relatively compacted state and the compacted state. Based on the operation steps described in Fig. 6, the construction methods of the five states can be explained as follows.

1) THE LOOSE STATE

We use a shovel to excavate an area of 20 cm-25 cm in the simulated lunar soil, and the simulated lunar soil is then scattered into the pit in a ''freefall'' method by shaking, that is, the backfilling mode 1 in Fig. 6. To ensure that the simulated lunar soil is in a loose state after backfilling, we use the clean-up scraper to scrape the backfilling and surrounding areas. The speed of the clean-up scraper is controlled at 10 cm/s.

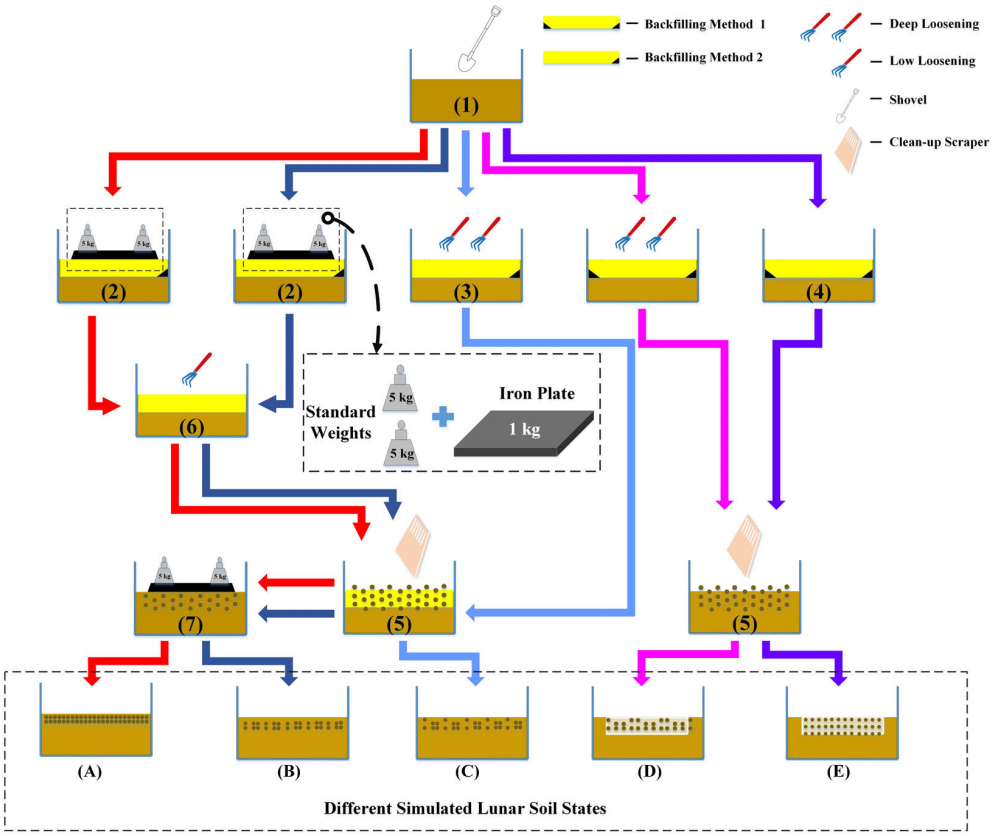

FIGURE 6. (A)-(E) The simulated lunar soil states: the compacted state, the relatively compacted state, the natural state, the relatively loose state, and the loose state; (1)-(7) The brief operation steps in this figure: (1) the excavation of simulated lunar soil; (2) the first standing operation; (3) deep loosening; (4) is different from (3) in based on whether the deep loosening operation is applied; (5) the flattening of the simulated lunar soil; (6) low loosening; (7) the second standing operation.

2) THE RELATIVELY LOOSE STATE

The processing steps for this state are similar to those of the loose state, and the difference is that a tine harrow is used for deep loosening (approximately 10 cm) in the backfilling area after backfilling. This operation is repeated 2-4 times in the horizontal and vertical directions.

3) THE NATURAL STATE

We use a shovel to excavate an area of 20 cm-25 cm in the simulated lunar soil. A section of simulated lunar soil with a width of less than 5 cm is longitudinally removed, rotated 180° and filled back into the vacant space in the simulated lunar soil, that is, the backfilling method 2 in Fig. 6. Then, the tine harrow is used for deep loosening (approximately 15 cm) in the backfilling area, and this operation is repeated 8-10 times in the horizontal and vertical directions. Finally, the clean-up scraper is used to scrape the backfilling area 2 to 3 times, and the speed is controlled at 10 cm/s.

4) THE RELATIVELY COMPACTED STATE

We use a shovel to excavate an area of 20 cm-25 cm in the simulated lunar soil according to the backfilling mode 2 in Fig. 6. Then, as shown in Fig. 6, an iron plate is placed on the simulated lunar soil, and its weight is 1 kg. In order to ensure that the simulated lunar soil is compacted, two standard 5 kg weights are placed on both ends of the iron plate, and the standing time is 5 hours. Next, the tine harrow is used for low loosening (approximately 10 cm), and the clean-up scraper is used for 2-3 rounds of flattening at a speed controlled at 10 cm/s. Finally, the steps for placing the iron plate and standard weights are repeated, but the standing time is approximately 2 hours.

5) THE COMPACTED STATE

The processing steps of the compacted state are similar to those of the relatively compacted state, but the difference is that the loosening depth is approximately 5 cm when the simulated lunar soil is loosened with the tine harrow, and the standing time in the final step is 10 hours.

After obtaining the above simulated lunar soil states, the reliability of the experiment could be fully guaranteed.

B. HARDNESS ANALYSIS IN DIFFERENT SOIL STATES

After completing the construction of the simulated lunar soil states, the simulated lunar rover is controlled to travel on the platform with the different simulated lunar soil states, which

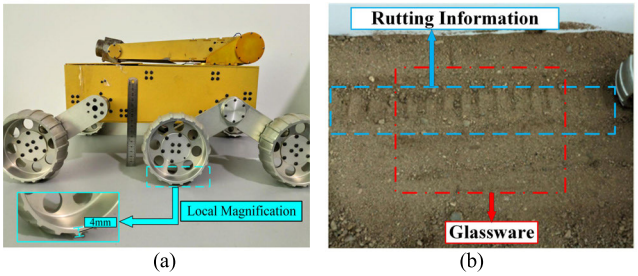

FIGURE 7. (a) Simulated lunar rover; (b) Rover rutting trace.

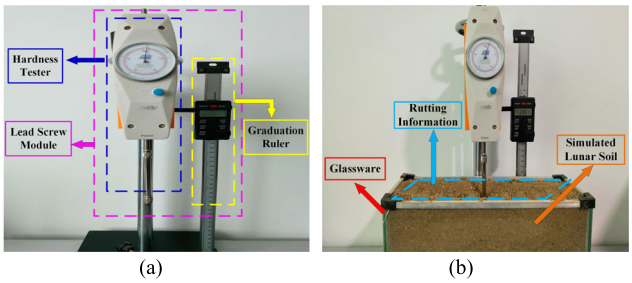

FIGURE 8. (a) Soil hardness measuring device; (b) Experiment platform of the hardness measurement.

left rutting traces. Then, we perform the static pressure test as shown in Fig. 7 and Fig. 8 to obtain the hardness value.

Under the existing conditions, we use the six-wheeled vehicle shown in Fig. 7(a) as the simulated lunar rover, and the thickness of each rover's wheel is 4 mm. The physical parameters of Yutu cannot be fully realized based on the existing conditions [6], but the speed, as one of the key factors, is easy to control. Therefore, the speed of the simulated lunar rover is the same as that of Yutu (200 m/h) to avoid interference due to movement, and this speed can be regarded as a low and uniform speed.

Moreover, Fig. 7(b) shows that the glassware with the simulated lunar soil is embedded in the soil of a given state before conducting the pressure tests and removed after the simulated lunar rover moved; these operations facilitate the implementation of the pressure test.

According to the standards mentioned by the American Society of Agricultural Engineers (ASAE) [45], the influence on the measurement accuracy can be ignored when the cone head is pushed into the soil at a low speed, and the penetration speed adopted by ASAE is 3.048 cm/s. In addition, when the pushing speed of the cone head is faster than 3 cm/ s, the value obtained by the hardness tester will be slightly higher than the actual value. When the pushing speed is equal to 1cm/s, the value obtained by the hardness tester is usually close to the actual value. Therefore, a screw module is combined with a soil hardness tester (see Fig. 8(a)) to control speed and depth.

Fig. 8(b) shows the recording of data after the glassware is removed. When measuring the simulated lunar soil hardness with the soil hardness tester, the cone head and probe rod should be vertically inserted as far as possible. The falling speed of the hardness tester should be controlled by the screw rod at 1 cm/s.

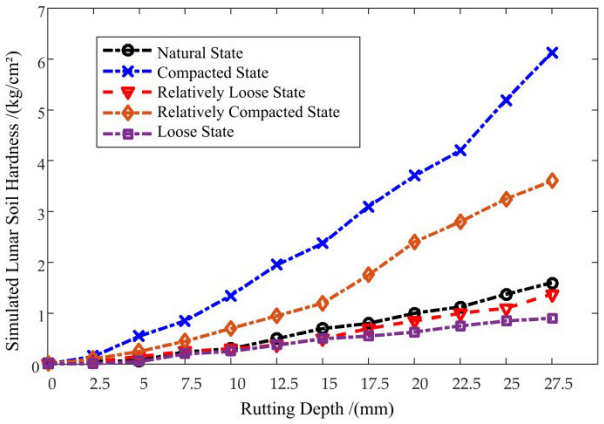

FIGURE 9. Hardness measurement results.

A total of ten collection points are randomly selected. In order to avoid the mutual influence of the collection points, we set a constraint: a circular area centred at the collection point and with a radius of 5 cm, cannot be used as the collection area for the next collection point.

When collecting the data, the penetration depth should also be controlled. In this paper, the depth value settings are 2.5 mm, 5 mm, 7.5 mm, ……, 27.5 mm, and the penetration depth value is monitored through the ruler in the lead screw module. By recording the hardness values at different penetration depths, it is possible to analyse the simulated lunar soil in different layers.

In Fig. 9, the results of the simulated lunar soil hardness measurements in five different states are shown. In the data fitting process, we consider the rutting surface depth to be 0 mm, and the hardness value of the rutting surface is 0 (kg/cm^2). Therefore, the empirical expressions between the depth value h (mm) and simulated lunar soil hardness y (kg/cm^2) can be obtained by fitting.

The empirical expression of the loose state is as follows:

$$y = -6.314 \times 10^{-3} - 2.21 \times 10^{-3}h + 4.7 \times 10^{-3}h^2 - 2.071 \times 10^{-4}h^3 + 3.03 \times 10^{-6}h^4. \quad (4)$$

The empirical expression of the relatively loose state is as follows:

$$y = 2.747 \times 10^{-3} + 2.209 \times 10^{-2}h + 7.792 \times 10^{-4}h^2 + 7.459 \times 10^{-6}h^3. \quad (5)$$

The empirical expression of the natural state is as follows:

$$y = -1.158 \times 10^{-2} + 1.49 \times 10^{-2}h + 2.297 \times 10^{-3}h^2 - 2.677 \times 10^{-5}h^3. \quad (6)$$

The empirical expression of the relatively compacted state is as follows:

$$y = -2.388 \times 10^{-2} + 8.345 \times 10^{-2}h - 8.838 \times 10^{-3}h^2 + 8.914 \times 10^{-4}h^3 - 1.841 \times 10^{-5}h^4. \quad (7)$$

The empirical expression of the compacted state is as follows:

$$y = -6.198 \times 10^{-2} + 1.028 \times 10^{-1}h + 3.68 \times 10^{-3}h^2 + 2.499 \times 10^{-5}h^3. \quad (8)$$

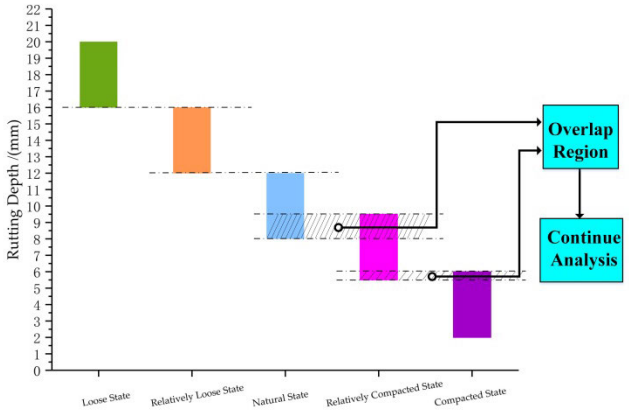

FIGURE 10. Relationships between the rutting depth and soil state.

C. ASSOCIATIONS OF THE RUTTING DEPTH AND SOIL STATE

When the simulated lunar soil state is known, the simulated lunar rover with a fixed load moves at a constant speed, and the rutting depth value can be approximately regarded as stable in a certain range. Therefore, we obtain the correlated rutting depth in the different simulated lunar soil states and propose relationships between the simulated lunar soil states and different rutting depths.

a) When the rutting depth is 16 mm-20 mm, the soil can be defined as being in the loose state;

b) When the rutting depth is 12 mm-16 mm, the soil can be defined as being in the relatively loose state;

c) When the rutting depth is 8 mm-12 mm, the soil can be defined as being in the natural state;

d) When the rutting depth is 5.5 mm-9.5 mm, the soil can be defined as being in the relatively compacted state;

e) When the rutting depth is 2 mm-6 mm, the soil can be defined as being in the compacted state.

In these different states, the rutting depth should be unique. Fig. 10 shows that the rutting depths have overlapping areas in the natural state, relatively compacted state and compacted state. There is no doubt that these overlapping areas will affect the determination of the simulated lunar soil state. To solve this problem, we use the following solution.

First, we address the measured value of the rutting depth by using a statistical method, and this method is as follows: At each area of overlap, a circular region with a radius of approximately 20 cm is created. In this area, we randomly select ten points and obtain the depths at these 10 points.

Secondly, the average depth value $\overline{x}$ of these points in the region is calculated, and the average $\overline{x}$ is compared with the thresholds in the three states. Therefore, the judgment conditions can then be defined as follows:

f) When 9.5 mm $< \overline{x} <$ 12 mm, the soil state in this area is defined as the natural state;

g) When 6 mm $< \overline{x} <$ 8 mm, the soil state in this area is defined as the relatively compacted state;

h) When 2 mm $< \overline{x} <$ 5.5 mm, the soil state in this area is defined as the compacted state.

If there are still overlapping ranges, we assume that the rutting depth in this area could be associated with more than one simulated lunar soil state, and their judgment conditions are defined as follows:

i) When 8 mm $< \overline{x} <$ 9.5 mm, the soil state in this area is defined as the natural state and the relatively compacted state;

j) When 5.5 mm $< \overline{x} <$ 6 mm, the soil state in this area is defined as the relatively compacted state and the compacted state.

According to the above ten defined judgment conditions for the simulated lunar soil state, we can correlate the rutting depth and the empirical formulas with the simulated lunar soil hardness. Firstly, the soil state is estimated according to the depth information obtained by the visual system, and then the hardness can be estimated by the corresponding hardness formula. In order to ensure the rationality and accuracy of these correlations, we consider the overlapping of the rutting depth values and propose solutions to this kind of problems. Therefore, we can use these connections to estimate the soil hardness.

IV. EXPERIMENTAL RESULTS

In this study, as a pivotal step in obtaining the rutting depth, the accuracy of the visual system measurement is extremely important. Therefore, in this section, the error of the vision measurement system is analysed first. The second experiment is verified from a simulation perspective, and the effectiveness and accuracy are analysed by comparing the measured values of the simulated lunar soil hardness obtained by our method with the actual values obtained by specialized instruments. Additionally, in the third experiment, the lunar surface images containing the rutting information retrieved by Yutu are used to estimate the lunar soil hardness value by using the proposed method to verify the feasibility.

A. ERROR ANALYSIS OF THE VISUAL MEASUREMENT SYSTEM

Our vision system consists of two MV-500SM/C industrial cameras, a fixed camera bracket and a computer with an Intel Core i7-4710MQ CPU and 8 GB of RAM. The highest resolution of the selected cameras is 2592 × 1944, and the frame rate is 7 fps. All data in this paper are processed on a 64-bit Win7 operating system, and the development and verification of the software are realized in MATLAB 2017b and Visual Studio 2010.

In the second section, we obtain the parameters of the camera via offline calibration. The principal points around the left and right cameras images are (1294.194, 980.395) and (1301.662, 979.451), respectively. The principal point are close to (1296, 972), which is half the camera maximum resolution. Fig. 11 shows the error values of the visual system calibration; the maximum errors are less than 0.11 pixels, and the overall mean error is only 0.09 pixels. In conclusion, the calibration results for the binocular vision system meet our needs.

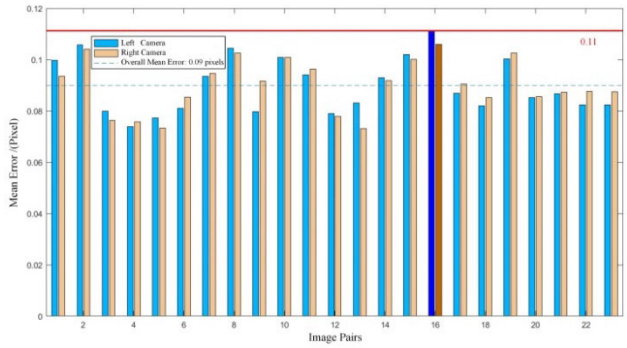

FIGURE 11. Camera calibration errors.

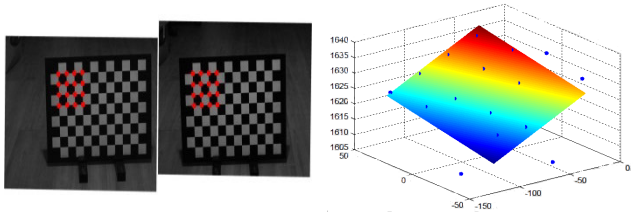

(a) (b)

FIGURE 12. (a) Selected points; (b) Fitting plane.

It is well known that measurement error can be estimated in many ways, but the rutting depth measurement method used in this paper principally depend on the precise estimation of three-dimensional coordinates. Therefore, the error of three-dimensional reconstruction is regarded as the measurement error in our visual system. To solve the problem that the external parameters of the camera on Yutu are unable to be measured, we adopt the calibration pattern images to estimate the systematic error. In Fig. 12(a), the accuracy of the calibration plate is only ± 0.01 mm, which is the ordinary level. If there is a higher requirement for accuracy, a superior level of the calibration board could be considered. Then, 16 colour-marked points on the calibration board are used to obtain three-dimensional coordinates via our visual measurements. Since the front surface of the calibration plate is relatively flat, these points are considered to be located in the same plane, and the fitting plane formula is $Z = 0.758X + 0.1617Y + 1637$, as shown in Fig. 12(b).

Finally, the average distance from all the marked points to the fitting plane is calculated and regarded as the measurement error of the vision system, with a value of 0.1141 mm. Combined with the calibration error of the system, the final overall system error is 0.1141 ± 0.01 mm. This error is below 1 mm; thus, the method can be used in complex and changeable environments.

B. HARDNESS MEASUREMENT BY USING SIMULATED RUTTING IMAGES

After the simulated lunar rover left traces on the simulated lunar soil, the rutting information is measured by using the method in Section II. Fig. 13(a) represents the collection of rutting images. Fig. 13(b) is the rutting feature matching result after completing a series of image processing

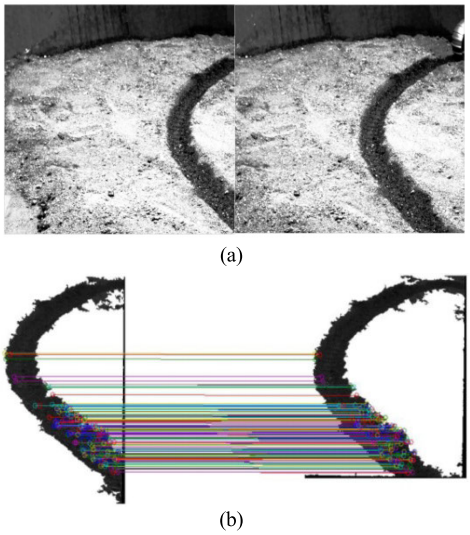

(a)

(b)

FIGURE 13. (a) Image acquisition in the simulated experiment; (b) Rutting feature matching.

steps designed in this paper. As mentioned in Section II, the rutting depth can be measured based on the three-dimensional rutting information. We select the ground coordinates from the pending three-dimensional coordinates to fit the ground surface plane, and the fitting plane formula is $Z = 2151.9153 - 1.0406X - 2.0653Y$.

Fifteen sample points are randomly selected from the rutting information, and the depths and three-dimensional coordinates are shown in Table 3.

According to the proposed judgment conditions in Section III, the soil states of these fifteen samples can be determined. The rutting depth values of sample 1 to sample 8, sample 12 and sample 15 are judged as the compacted state based on the judgment condition (e). According to condition (f), the depth values of sample 9 to sample 11 and sample 14 are identified as the relatively compacted state. In particular, the value for sample 13 is 5.8237 mm, which is within the overlapping regions mentioned in Section III, so it is necessary to obtain the matching results of the characteristic points associated with the sample and calculate the mean rutting depth corresponding to the matching results. After retrieving this information, sample 13 has only one matching point, and its value is 5.3052 mm. Therefore, the depth value of sample 13 can be updated to 5.5644 mm. According to the judgment condition (j), 5.5644 mm is within the range of [5.5 mm, 6 mm], and sample 13 can be determined as the compacted state and the relatively compacted state.

For intuitive comparison, all the sample points are processed with the corresponding empirical formula after determining the soil states, and the results are shown in Table 4. In these data, the actual values are obtained by precise instruments, and the measured values are calculated by our algorithms. We can see that the measured values based on the rutting images are largely consistent with the actual values. Fig. 14 can be used to assess the accuracy of the

TABLE 3. Measurement of the rutting depth by using simulated experimental images.

Serial Number	Three-dimensional Coordinates			Measured (mm)
	X	Y	Z	
1	270.09	118.36	1635.50	3.6074
2	255.61	107.49	1676.55	5.0094
3	285.89	107.79	1636.21	1.7505
4	235.61	88.88	1728.25	2.0140
5	232.54	92.21	1728.95	3.7534
6	248.99	100.95	1690.31	2.3757
7	273.35	121.83	1627.16	4.4881
8	283.10	113.2	1631.66	3.2270
9	221.05	94.35	1743.44	6.5131
10	280.06	142.10	1582.89	6.3043
11	186.81	32.59	1906.23	6.3571
12	231.80	68.96	1770.49	0.8767
13	218.19	63.86	1807.65	5.8237
14	197.89	57.37	1845.02	6.9517
15	210.16	42.88	1851.94	2.8882

TABLE 4. Soil hardness measurement using the specialized instrument and vision-based method.

Serial Number	Rutting depth (mm)	Hardness of Simulated Lunar Soil	
		Measured (kg/cm^2)	Actual (kg/cm^2)
1	3.6074	0.3579	0.3750
2	5.0094	0.5485	0.5500
3	1.7505	0.1294	0.1500
4	2.0140	0.1602	0.2250
5	3.7534	0.3770	0.4000
6	2.3757	0.2033	0.2500
7	4.4881	0.4757	0.4700
8	3.2270	0.3089	0.3100
9	6.5131	0.3578	0.3600
10	6.3043	0.3452	0.3400
11	6.3571	0.3483	0.3500
12	0.8767	0.0310	0.0500
13	5.8237	0.6664/0.3173	0.6100/0.3000
14	6.9517	0.3856	0.4200
15	2.8882	0.2662	0.2600

method proposed in this paper. It is worth noting that the rutting depth of sample 13 meets the judgment condition (j), so we calculate the hardness values of the two soil states. As shown in Fig. 14, sample 13 can be divided into states A and B, which represent the compacted state and the relatively compacted state, respectively. We take the mean value of the errors of the two states as the sample error value. Fig. 14 shows that the errors of the hardness values measured by our method are very small; notably, the maximum error is 0.0648 mm, and the average deviation is only 0.0189 mm. In short, the error of our method can meet the requirements of practical applications.

C. HARDNESS MEASUREMENT BY USING RUTTING IMAGES FROM Yutu

To evaluate the feasibility of our method in a real environment, real images with rutting information from Yutu and known camera parameters are used for image processing. The processing results of these steps are covered in Section II. We select the ground coordinates from the pending three-dimensional coordinates to fit the lunar surface plane, and the fitting plane formula is $Z = 8.247 \times 10^4 + 2.984X = 2.512Y$. Then, the steps after the points fitting are similar to those of the ground simulated experiment. Five random sample points

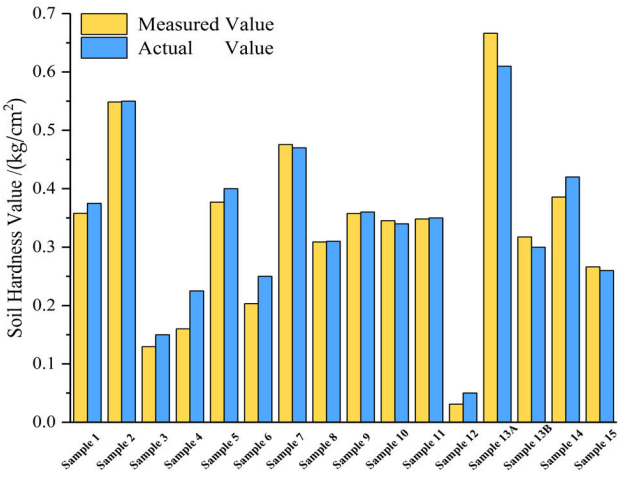

FIGURE 14. Comparison between the measured results and actual results.

TABLE 5. Measurement of the rutting depth by using images from Yutu.

Serial Number	Three-dimensional Coordinates			Rutting Depth Measurement (mm)
	X	Y	Z	
1	22308.14	-1317.70	152513.87	41.3036
2	17644.58	214.05	134310.83	67.7732
3	7557.12	5501.88	91112.61	21.6339
4	7988.92	5258.39	92989.96	27.2931
5	3914.57	7711.08	74490.01	72.2262

are chosen, and the corresponding three-dimensional coordinates and rutting depths are reported in Table 5. Clearly, the minimum value of the rutting depths for these sample points is 21.6339 mm; however, under the judgment conditions, the value of the rutting depth may have different states only when the value is lower than 20 mm. In other words, the soil state can be determined by utilizing the defined conditions, and the corresponding empirical formulas can be applied to measure the soil hardness. The lunar soil state can be determined as the loose state when the rutting depth value is higher than 20 mm, and the soil hardness can be measured by using the corresponding empirical formula (see equation (5)). Therefore, the soil hardness values of all sample points in this case are 2.1461, 20.8881, 0.7124, 0.9052 and 28.7776 (kg/cm^2). In a word, we can estimate the lunar soil hardness by using images from the actual work environment.

V. CONCLUSION AND PROSPECT

In this paper, we propose a noncontact method that can measure the lunar soil hardness by using rutting images. Our method includes a vision-based rutting depth measurement system and a soil hardness measurement system. Specifically, the soil hardness measurement system essentially obtains empirical formulas through ground experiments and completes the estimation of soil hardness by combination with rutting depth information. To better simulate a real lunar environment, five different simulated lunar soil states are created.

The main contributions of this paper are as follows. (1) Different from the general estimation of lunar soil parameters, our method focuses on the soil hardness parameter; this approach can replace the special sensor to save more space and reduce energy consumption to some extent. (2) We apply the designed visual algorithm to estimate soil hardness, which can realize the reuse of existing sensor data. (3) We design a set of economical and simple ground simulation schemes that ensure the accuracy and feasibility of the hardness measurement system. Additionally, we define ten judgment conditions of the soil state based on the rutting depth and the empirical formulas of soil hardness based on different soil states. The experimental results show that our method can estimate the soil hardness parameter from both simulated rutting images and real lunar rutting images, and the measured results have high accuracy in the simulated experiment. Therefore, this method has high engineering application value and could be used for soil hardness analysis during the operation of a lunar rover.

However, the rutting images used in this paper are collected in the normal lunar environment, and further studies are needed to consider more complex lunar work environments. In addition, this paper mainly performs qualitative analysis tasks; future work will focus on quantitative studies, optimizing the method and further improving the accuracy of the method.

REFERENCES

[1] D. Liu, L. Li, and Y. Sun, "An improved radiative transfer model for estimating mineral abundance of immature and mature lunar soils," *Icarus*, vol. 253, pp. 40–50, Jun. 2015, doi: 10.1016/j.icarus.2015.02.013.

[2] S. Li, P. Cui, and H. Cui, "Vision-aided inertial navigation for pinpoint planetary landing," *Aerosp. Sci. Technol.*, vol. 11, no. 6, pp. 499–506, Sep. 2007, doi: 10.1016/j.ast.2007.04.006.

[3] X. Mao, J. Chen, Y. Xing, B. Teng, X. Liu, and Y. Jia, "Lunar rover's vision technology for auto-navigation," in *Proc. 33rd Chin. Control Conf.*, Jul. 2014, pp. 864–868, doi: 10.1109/ChiCC.2014.6896741.

[4] G. Reina, G. Ishigami, K. Nagatani, and K. Yoshida, "Odometry correction using visual slip angle estimation for planetary exploration rovers," *Adv. Robot.*, vol. 24, no. 3, pp. 359–385, Jan. 2010, doi: 10.1163/016918609X12619993300548.

[5] J. J. Halvorson, D. K. McCool, L. G. King, and L. W. Gatto, "Soil compaction and over-winter changes to tracked-vehicle ruts, Yakima Training Center, Washington," *J. Terramech.*, vol. 38, no. 3, pp. 133–151, Jul. 2001, doi: 10.1016/S0022-4898(00)00017-3.

[6] C. Li, J. Liu, X. Ren, W. Zuo, X. Tan, W. Wen, H. Li, L. Mu, Y. Su, H. Zhang, J. Yan, and Z. Ouyang, "The Chang'e 3 mission overview," *Space Sci. Rev.*, vol. 190, nos. 1–4, pp. 85–101, Jul. 2015, doi: 10.1007/s11214-014-0134-7.

[7] X. Zhang, J. Liu, Q. Gao, and Z. Ju, "Adaptive robust decoupling control of multi-arm space robots using time-delay estimation technique," *Nonlinear Dyn.*, vol. 100, no. 3, pp. 2449–2467, May 2020, doi: 10.1007/s11071-020-05615-5.

[8] X. Zhang, J. Liu, J. Feng, Y. Liu, and Z. Ju, "Effective capture of nongraspable objects for space robots using geometric cage pairs," *IEEE/ASME Trans. Mechatronics*, vol. 25, no. 1, pp. 95–107, Feb. 2020, doi: 10.1109/TMECH.2019.2952552.

[9] Y. Gao, C. Spiteri, C.-L. Li, and Y.-C. Zheng, "Lunar soil strength estimation based on Chang'E-3 images," *Adv. Space Res.*, vol. 58, no. 9, pp. 1893–1899, Nov. 2016, doi: 10.1016/j.asr.2016.07.017.

[10] D.-Y. Wang, Y.-L. Zhu, W. Ma, and Y.-H. Niu, "Application of ultrasonic technology for physical–mechanical properties of frozen soils," *Cold Regions Sci. Technol.*, vol. 44, no. 1, pp. 12–19, Jan. 2006, doi: 10.1016/j.coldregions.2005.06.003.

[11] J. R. Johnson, M. K. Shepard, W. M. Grundy, D. A. Paige, and E. J. Foote, "Spectrogoniometry and modeling of martian and lunar analog samples and apollo soils," *Icarus*, vol. 223, no. 1, pp. 383–406, Mar. 2013, doi: 10.1016/j.icarus.2012.12.004.

[12] L. Ding, H. Gao, Z. Liu, Z. Deng, and G. Liu, "Identifying mechanical property parameters of planetary soil using *in-situ* data obtained from exploration rovers," *Planet. Space Sci.*, vol. 119, pp. 121–136, Dec. 2015, doi: 10.1016/j.pss.2015.09.003.

[13] M. Cross, A. Ellery, and A. Qadi, "Estimating terrain parameters for a rigid wheeled rover using neural networks," *J. Terramechan.*, vol. 50, no. 3, pp. 165–174, Jun. 2013, doi: 10.1016/j.jterra.2013.04.002.

[14] W. Xiao and Y. Zhang, "Design of manned lunar rover wheels and improvement in soil mechanics formulas for elastic wheels in consideration of deformation," *J. Terramech.*, vol. 65, pp. 61–71, Jun. 2016, doi: 10.1016/j.jterra.2016.03.004.

[15] K. Iagnemma, C. Brooks, and S. Dubowsky, "Visual, tactile, and vibration-based terrain analysis for planetary rovers," in *Proc. IEEE Aerosp. Conf. Process.*, Mar. 2004, pp. 841–848, doi: 10.1109/AERO.2004.1367684.

[16] M. Li, F. Gao, P. Sun, and Y. Cui, "The algorithm research of Terrain parameter estimation based on lunar rover's traveling information," in *Proc. Int. Conf. Optoelectron. Image Process.*, vol. 2, Nov. 2010, pp. 502–506, doi: 10.1109/ICOIP.2010.38.

[17] J.-Y. Wong and A. R. Reece, "Prediction of rigid wheel performance based on the analysis of soil-wheel stresses: Part II. Performance of towed rigid wheels," *J. Terramechan.*, vol. 4, no. 2, pp. 7–25, Jan. 1967, doi: 10.1016/0022-4898(67)90047-X.

[18] T. Kage and K. Matsushima, "Method of rut detection using lasers and in-vehicle stereo camera," in *Proc. Int. Conf. Intell. Informat. Biomed. Sci. (ICIIBMS)*, Nov. 2015, pp. 48–53, doi: 10.1109/ICIIBMS.2015.7439479.

[19] A. E. Kenarsari, S. J. Vitton, and J. E. Beard, "Creating 3D models of tractor tire footprints using close-range digital photogrammetry," *J. Terramechan.*, vol. 74, pp. 1–11, Dec. 2017, doi: 10.1016/j.jterra.2017.06.001.

[20] T. Botha, D. Johnson, S. Els, and S. Shoop, "Real time rut profile measurement in varying terrain types using digital image correlation," *J. Terramechan.*, vol. 82, pp. 53–61, Apr. 2019, doi: 10.1016/j.jterra.2018.12.003.

[21] H. Gao, J. Guo, L. Ding, N. Li, Z. Liu, G. Liu, and Z. Deng, "Longitudinal skid model for wheels of planetary exploration rovers based on Terramechanics," *J. Terramechan.*, vol. 50, nos. 5–6, pp. 327–343, Oct. 2013, doi: 10.1016/j.jterra.2013.10.001.

[22] L. Xue, J. Li, M. Zou, W. Zong, and H. Huang, "*in situ* identification of shearing parameters for loose lunar soil using least squares support vector machine," *Aerosp. Sci. Technol.*, vol. 53, pp. 154–161, Jun. 2016, doi: 10.1016/j.ast.2016.03.018.

[23] Y. Gao and J. Liu, "China's robotics successes abound," *Science*, vol. 345, no. 6196, p. 523, 2014, doi: 10.1126/science.345.6196.523-a.

[24] Y. Jia, "Chang'E-3 Lander's Scientific Payloads," *Chin. J. Space Sci.*, vol. 34, no. 2, pp. 219–225, 2014.

[25] J. Lai, Y. Xu, X. Zhang, and Z. Tang, "Structural analysis of lunar subsurface with ChangŒşE-3 lunar penetrating radar," *Planet. Space Sci.*, vol. 120, pp. 96–102, Jan. 2016, doi: 10.1016/j.pss.2015.10.014.

[26] Y. Jia, Y. Zou, J. Ping, C. Xue, J. Yan, and Y. Ning, "The scientific objectives and payloads of chang'E' 4 mission," *Planet. Space Sci.*, vol. 162, pp. 207–215, Nov. 2018, doi: 10.1016/j.pss.2018.02.011.

[27] S. Gou, K. Di, Z. Yue, Z. Liu, Z. He, R. Xu, B. Liu, M. Peng, W. Wan, Y. Wang, and J. Liu, "Forsteritic olivine and magnesium-rich orthopyroxene materials measured by Chang'e-4 rover," *Icarus*, vol. 345, Jul. 2020, Art. no. 113776, doi: 10.1016/j.icarus.2020.113776.

[28] Y. Jia, S. Dai, Y. Zou, and X. Chen, "An overview of the scientific payloads in chinese Chang'e-3 lunar mission," in *Proc. IEEE Int. Geosci. Remote Sens. Symp. (IGARSS)*, Jul. 2016, pp. 3715–3718, doi: 10.1109/IGARSS.2016.7729963.

[29] R. Juarez-Salazar and V. H. Diaz-Ramirez, "Flexible camera-projector calibration using superposed color checkerboards," *Opt. Lasers Eng.*, vol. 120, pp. 59–65, Sep. 2019, doi: 10.1016/j.optlaseng.2019.02.016.

[30] D. Li and J. Tian, "An accurate calibration method for a camera with telecentric lenses," *Opt. Lasers Eng.*, vol. 51, no. 5, pp. 538–541, May 2013, doi: 10.1016/j.optlaseng.2012.12.008.

[31] S. Zhang, S. Liu, Y. Ma, C. Qi, H. Ma, and H. Yang, "Self calibration of the stereo vision system of the Chang'e-3 lunar rover based on the bundle block adjustment," *ISPRS J. Photogramm. Remote Sens.*, vol. 128, pp. 287–297, Jun. 2017, doi: 10.1016/j.isprsjprs.2017.04.004.

[32] M. Ito, "Robot vision modelling-camera modelling and camera calibration," *Adv. Robot.*, vol. 5, no. 3, pp. 321–335, Jan. 1990, doi: 10.1163/156855391X00232.
[33] O. Faugeras and G. Toscani, "The calibration problem for stereo," in *Proc. IEEE Conf. Comput. Vis. Pattern Recognit.*, Oct. 1986, vol. 42, no. 12, pp. 195–213.
[34] R. Tsai, "A versatile camera calibration technique for high-accuracy 3D machine vision metrology using off-the-shelf TV cameras and lenses," *IEEE J. Robot. Autom.*, vol. 3, no. 4, pp. 323–344, Aug. 1987, doi: 10.1109/JRA.1987.1087109.
[35] Z. Zhang, "A flexible new technique for camera calibration," *IEEE Trans. Pattern Anal. Mach. Intell.*, vol. 22, no. 11, pp. 1330–1334, Feb. 2000, doi: 10.1109/34.888718.
[36] L. Wu and B. Zhu, "Binocular stereovision camera calibration," in *Proc. IEEE Int. Conf. Mechatronics Autom. (ICMA)*, Aug. 2015, pp. 2638–2642, doi: 10.1109/ICMA.2015.7237903.
[37] L. Huang, W. Zhao, B. R. Abidi, and M. A. Abidi, "A constrained optimization approach for image gradient enhancement," *IEEE Trans. Circuits Syst. Video Technol.*, vol. 28, no. 8, pp. 1707–1718, Aug. 2018, doi: 10.1109/TCSVT.2017.2696971.
[38] S. Patel and M. Goswami, "Comparative analysis of histogram equalization techniques," in *Proc. Int. Conf. Contemp. Comput. Informat. (ICI)*, Nov. 2014, pp. 167–168, doi: 10.1109/IC3I.2014.7019808.
[39] M. Dadgar, S. Jafari, and A. Hamzeh, "A PSO-based multi-robot cooperation method for target searching in unknown environments," *Neurocomputing*, vol. 177, pp. 62–74, Feb. 2016, doi: 10.1016/j.neucom.2015.11.007.
[40] Z. Jianjun, Y. Heng, G. Xiaoguang, and W. Sheng, "The edge detection of river model based on self-adaptive Canny Algorithm and connected domain segmentation," in *Proc. 8th World Congr. Intell. Control Automat.*, Jul. 2010, pp. 1333–1336, doi: 10.1109/WCICA.2010.5554869.
[41] A. Fusiello, E. Trucco, and A. Verri, "A compact algorithm for rectification of stereo pairs," *Mach. Vis. Appl.*, vol. 12, no. 1, pp. 16–22, Jul. 2000, doi: 10.1007/s001380050120.
[42] W. Burger and M. J. Burge, "Scale-invariant feature transform (SIFT)," in *Digital Image Processing: An Algorithmic Introduction Using Java*, W. Burger and M. J. Burge Eds. London, U.K.: Springer, 2016, pp. 609–664.
[43] H. Bay, A. Ess, T. Tuytelaars, and L. Van Gool, "Speeded-up robust features (SURF)," *Comput. Vis. Image Understand.*, vol. 110, no. 3, pp. 346–359, Jun. 2008, doi: 10.1016/j.cviu.2007.09.014.
[44] E. Rublee, V. Rabaud, K. Konolige, and G. Bradski, "ORB: An efficient alternative to SIFT or SURF," in *Proc. Int. Conf. Comput. Vis.*, Nov. 2011, pp. 2564–2571, doi: 10.1109/ICCV.2011.6126544.
[45] J. L. Hernanz, H. Peixoto, C. Cerisola, and V. Sánchez-Girón, "An empirical model to predict soil bulk density profiles in field conditions using penetration resistance, moisture content and soil depth," *J. Terramech.*, vol. 37, no. 4, pp. 167–184, Jan. 2000, doi: 10.1016/S0022-4898(99)00020-8.

HONGWEI GAO received the Ph.D. degree in the field of pattern recognition and intelligent system from the Shenyang Institute of Automation (SIA), Chinese Academy of Sciences (CAS), in 2007. Since September 2015, he has been a Professor with the School of Automation and Electrical Engineering, Shenyang Ligong University. He is currently the Leader of academic direction for optical and electrical measuring technology and system. His research interests include digital image processing and analysis, stereo vision, and intelligent computation. He has published more than 60 technical articles in these areas as first authors or coauthors.

YUQI ZHOU was born in Liaoning, China, in 1995. He received the B.S. degree from Shenyang Ligong University, China, in 2018, where he is currently pursuing the M.S. degree. His research interests include machine vision and image processing.

YUEQIU JIANG received the Ph.D. degree in computer application technology from Northeastern University, in 2004. Since 2010, she has been a Full Professor with Shenyang Ligong University. She is currently the Leader of subject direction for signal and information process. Her research interests include network management and image processing.

JIAHUI YU received the B.S. and M.S. degrees (with major in intelligent systems) from Shenyang Ligong University, China, in 2017 and 2019, respectively. He is currently pursuing the Ph.D. degree with the University of Portsmouth, U.K. His current research interests include machine intelligence, pattern recognition, and human–robot/computer interaction and collaboration.

ZHAOJIE JU (Senior Member, IEEE) received the B.S. degree in automatic control and the M.S. degree in intelligent robotics from the Huazhong University of Science and Technology, China, and the Ph.D. degree in intelligent robotics from the University of Portsmouth, U.K. He held research appointments at University College London, London, U.K., before he started his independent academic position at the University of Portsmouth, in 2012. He has authored or coauthored over 180 publications in journals, book chapters, and conference proceedings. His research interests include machine intelligence, pattern recognition and their applications on human motion analysis, multi-fingered robotic hand control, human–robot interaction and collaboration, and robot skill learning. He received four Best Paper Awards and one Best AE Award in ICRA2018. He is also an Associate Editor of the IEEE TRANSACTIONS ON CYBERNETICS, the IEEE TRANSACTIONS ON COGNITIVE AND DEVELOPMENTAL SYSTEMS, IEEE ACCESS, and *Neurocomputing*.

JINGUO LIU (Senior Member, IEEE) received the Ph.D. degree in mechatronics from the Shenyang Institute of Automation (SIA), Chinese Academy of Sciences (CAS), in 2007. He has been a Full Professor with SIA, CAS, since January 2011, the Assistant Director of the State Key Laboratory of Robotics, since 2008, and the Associate Director of the Center for Space Automation Technologies and Systems, since 2015. His research interests include bio-inspired robotics and space robot. He has authored or coauthored three books, over 100 articles, and holds 50 patents in above areas. He is a Senior Member of the IEEE Technical Committee on Safety, Security, and Rescue Robotics, the IEEE Technical Committee on Marine Robotics, and the Chinese Mechanical Engineering Society. He was a recipient of the T. J. TARN Best Paper Award in Robotics from the 2005 IEEE International Conference on Robotics and Biomimetics, the Best Paper Award of the Chinese Mechanical Engineering Society, in 2007, the Best Paper Nomination Award from the 2008 International Symposium on Intelligent Unmanned Systems, the Best Paper Award from the 2016 China Manned Space Academic Conference, the Outstanding Paper Award from the 2017 International Conference on Intelligent Robotics and Applications, and the Best Paper Award from the 2018 International Conference on Electrical Machines and Systems. He serves as an Associate Editor or Technical Editor for several journals, such as the IEEE/ASME TRANSACTIONS ON MECHATRONICS, IEEE ACCESS, *Mechanical Sciences*, *Science China Technological Sciences*, the *Chinese Journal of Mechanical Engineering*, and the *Chinese Journal of Aeronautics*.